

Arrokoth's Necklace

J. I. Katz^{1*} and S. Wang²

¹Department of Physics and McDonnell Center for the Space Sciences, Washington University, St. Louis, Mo. 63130 USA

²Department of Physics, Washington University, St. Louis, Mo. 63130 USA

9 March 2021

ABSTRACT

Flyby images of (486958) Arrokoth (Ultima Thule, 2014 MU₆₉) show a comparatively bright “necklace” in the neck, or cleft, between its two lobes, in contrast to its generally low albedo. We suggest that the necklace may be the result of thermally controlled ice deposition. The necklace is found in the most (orbitally averaged) shaded part of the surface. It may consist of clean, high albedo, ice condensed from vapor sublimed by dirty, low albedo, ice elsewhere; ice accumulates where the *maximum* temperatures are the lowest. Ammonia and propane have the necessary mesovolatile vapor pressure. Surrounding gas in the proto-Solar System would facilitate redeposition of molecules sublimed by warmer parts of the surface into the cleft, as well as smoothing the surface and explaining, by hydrodynamic drag, Arrokoth's slow (compared to its breakup rate) rotation. Alternatively, a layer of hoarfrost thick enough ($\gtrsim 0.1 \mu$) to have a high albedo could have formed more recently.

Key words: Kuiper Belt Objects: (486958) Arrokoth, 2014 MU₆₉, Ultima Thule

1 INTRODUCTION

(486958) Arrokoth (Ultima Thule, 2014 MU₆₉) (Stern *et al.* 2019; Grundy *et al.* 2020; McKinnon *et al.* 2020; Spencer *et al.* 2020), a cold classical Kuiper belt object, became the most distant object visited by a spacecraft following the flyby by New Horizons January 1, 2019. Imaging (McKinnon *et al.* 2020) revealed it to be a contact binary consisting of two lobes with equivalent diameters of about 19 and 14 km, rotating with a period of 15.92 h. Its location in the outer Solar System with orbital semi-major axis $a = 44.6$ AU and eccentricity $e = 0.042$ (Porter *et al.* 2018; Stern *et al.* 2019) suggests a predominantly icy composition, although its low (compared to those of pure ices) albedo ≈ 0.06 (Hofgartner *et al.* 2021) implies some mineral (“dirt”) admixture with the mineral matter frozen into a continuous icy matrix¹ or a surface of photochemically processed tholins.

* E-mail: katz@uphys.wustl.edu

¹ If there were voids between particles of clean ice Arrokoth would resemble snow that has high albedo as a result of scattering of light at the surfaces of the transparent ice particles, unless mineral matter constitutes a substantial fraction of its volume. Comparison of the observed albedo to that of the presumptive mineral content may constrain its microstructure: very small ($\ll \lambda$, the wavelength of visible light) mineral particles frozen into the ice without voids would produce a dirty ice albedo less than that of macroscopic solids. This may be demonstrated by adding water to granular sugar with about 10^{-4} admixture of carbon black: Without water, the mixture is light grey, but adding water reduces the discontinuity in refractive index at the sugar grains, producing a black slurry. A mixture of ices and larger mineral particles, even without voids, has an albedo larger than that of bulk mineral because of scattering from the surface of the ice.

The most striking feature of images of Arrokoth is a bright ring or “necklace” where the two lobes are in contact. This paper proposes that the necklace is produced by thermal evaporation of ice, likely ammonia ice, from the most strongly heated portions of the surface and the deposition of some fraction of it on the neck, the most shaded and coolest portion. Deposition from the vapor would produce a layer of nearly pure solid ice with high albedo. Brighter regions in apparent craters and other surface depressions may have a similar origin. Lisse *et al.* (2021); Steckloff *et al.* (2021) have discussed the presence of hyper- and refractory volatiles in Arrokoth and their effects on its bulk evolution and spin-down, but have not addressed the question of moderately volatile, metastable or mesostable ices and its bright “necklace”. The neck is a low of both *peak* temperatures, because it is shaded from sunlight at most times, and of gravitational potential, because it is near the center of mass. Material may be deposited there by condensation or by gravitational flow; this paper is concerned with the former hypothesis.

The peculiar shape of Arrokoth, consisting of two smooth lobes in contact with a narrow cleft between them, rotating well below their break-up rate, also requires explanation: Why did the process that smoothed the lobes not fill in the cleft? This paper proposes that the lobes formed and smoothed in the gas-filled proto-Solar System. Bodies immersed in gas that prevents the free escape of sublimed material smooth by evaporation from the convex and warmest parts of their Solar-heated surfaces and recondensation on cooler, shadowed, concave parts. Drag from immersing gas also slows the rotation of a contact binary, possibly explaining the shedding of angular momentum required to produce the slowly spinning bilobate object seen to

day (Lyra, Youdin & Johansen 2021; McKinnon *et al.* 2020; Steckloff *et al.* 2021).

2 HEAT FLOW

2.1 Steady State

The steady state daytime temperature of a grey (equal albedos and emissivities for Solar and thermal radiation) surface, considering only local radiation absorption and emission, is

$$T_{\text{steady}} = (I_{\odot} \sin \theta / \sigma_{SB})^{1/4}, \quad (1)$$

where I_{\odot} is the Solar intensity, $0 \leq \theta \leq \pi/2$ the grazing angle of the Sun's rays to the surface and σ_{SB} the Stefan-Boltzmann constant. For $\theta = \pi/2$ (Sun at the zenith) this varies around the orbit from 58.4 K to 60.6 K.

In fact, these extreme temperatures are not achieved because of conduction to and from the interior of the body. The deep interior of a grey sphere comes to the mean temperature

$$\langle T \rangle = (I_{\odot} / 4\sigma_{SB})^{1/4} \approx 42 \text{ K}. \quad (2)$$

The grey-body temperature can only be an approximation to the steady state surface temperature. Actual steady state temperatures are a factor $[(1 - A_{\odot}) / (1 - A_{\text{thermal}})]^{1/4}$ times the grey body values, where $A_{\odot} \approx 0.06$ (Stern *et al.* 2019; Hofgartner *et al.* 2021) is the spectral-, polarization- and angular-averaged bolometric Solar albedo (insufficient information exists to determine this precisely) and $1 - A_{\text{thermal}}$ is the emissivity, similarly averaged over the Planck function at the surface temperature. For pure, clean NH₃ ice at relevant temperatures $1 - A_{\text{thermal}} \approx 0.77$ (Appendix), possibly increased by the presence of mineral "dirt" or a surface layer of tholins. Steady state temperatures of clean NH₃ ice are therefore expected to be about 5% higher than those of a grey body, a correction that is not included explicitly here because it is not large and because of its uncertainty.

2.2 Transients

The surface of Arrokoth is not in thermal steady state. Several time scales enter: the short ($P_{\text{rot}} = 15.92$ h) rotation period, the longer ($P_{\text{orb}} = 298$ y) orbital period, the thermal conduction time scale of the body as a whole ($t_{\text{deep}} \sim 3 \times 10^5$ y) and the evolution time scale ($t_{\odot} \sim 5 \times 10^9$ y) of the Solar luminosity, which is approximately the age of Arrokoth. The rotation axis is only 9° from the orbital plane (Grundy *et al.* 2020), so that most portions of the surface are continuously sunlit and then continuously dark, each for a substantial fraction of the 298 y orbital period. This produces temperature excursions about the mean $\langle T \rangle$.

There is yet another characteristic time scale. As the insolation varies with the rotational and orbital cycles, Solar heating and thermal radiation cooling of the surface compete with conductive heat flow into or out of the interior as sinks or sources of energy. In a time Δt the thermal diffusion wave penetrates a distance

$$\Delta x \approx \sqrt{\mathcal{K} \Delta t / (C_{p,s} \rho)}, \quad (3)$$

where $C_{p,s}$ is the heat capacity (per unit mass) of the solid, ρ its density and \mathcal{K} its thermal conductivity, carrying an energy per unit area $C_{p,s} \rho \Delta T \Delta x$, while the surface absorbs and

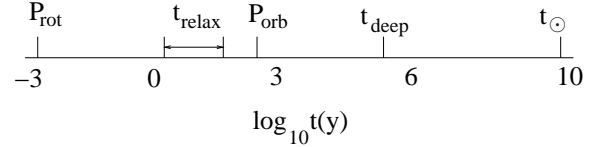


Figure 1. Characteristic time scales. The range for t_{relax} corresponds to the range of possible compositions, with shorter values for low-conductivity materials like glassy CH₃OH or snows, and longer values for water ice.

emits $\sim I_{\odot} \Delta t$. Equating these energies defines the characteristic thermal relaxation time of the surface

$$t_{\text{relax}} \equiv \frac{(\Delta T)^2 C_{p,s} \rho \mathcal{K}}{I_{\odot}^2} \approx 1.5 \times 10^9 \text{ s} \approx 50 \text{ y} \quad (4)$$

and

$$\Delta x \approx \frac{\mathcal{K} \Delta T}{I_{\odot}} \approx 130 \text{ m}, \quad (5)$$

where we have taken the heat capacity and thermal conductivity to be those of solid NH₃ (Popov, Manzhelii & Bagatskii 1971; Krupskii, Manzhely & Koloskova 1968). Most other ices (water ice (Giauque & Stout 1936) and CO₂ ice (Giauque & Egan 1937)) have similar values, while the thermal conductivity of CH₃OH is about 30 times less (Korolyuk *et al.* 2009) and its t_{relax} and Δx are correspondingly less. Changes in irradiation on shorter time scales have little effect on the surface temperature, while on time scales (such as the orbital period) between t_{relax} and t_{deep} the surface temperature relaxes to the mean insolation.

The several time scales are ordered

$$P_{\text{rot}} \ll t_{\text{relax}} \lesssim P_{\text{orb}} \ll t_{\text{deep}} \ll t_{\odot}. \quad (6)$$

These inequalities are illustrated in Fig. 1. The strong inequalities simplify the analysis by separating the time scales on which some processes are insignificant while others have gone to completion. The rotational slowing time t_{slow} is not included in these inequalities because it increases by many orders of magnitude as the protoplanetary nebula dissipates, so that at present it far exceeds t_{\odot} , while during the period of most efficient (diffusive) vapor transfer from warmer regions to the neck (Sec. 5.2) it is less than t_{\odot} , although not by orders of magnitude.

The rotation axis is only 9° from the orbital plane (Grundy *et al.* 2020). On time scales $\gg t_{\text{relax}}$ thermal conduction is unimportant and surface temperatures relax to the steady state values corresponding to their mean insolation. On shorter time scales conduction is important, the internal specific heat acts as thermal ballast, and temperature varies less than it would on longer time scales. Rotational modulation of insolation produces only small variation of surface temperature; the surface temperature is nearly constant at the value corresponding to the rotationally averaged insolation (which, in general, is not the deep interior $\langle T \rangle$). Relaxation to the radiative equilibrium temperature is, at best, approximate for the orbital (seasonal) cycle.

For a slab of thickness r (a fair approximation to the highly flattened shape of Arrokoth's lobes) with radiatively heated temperature T that varies by ΔT across its surface, the ratio of conductive heat flow from warmer parts of the surface

through the deep interior to its black body radiation is, *in steady state*,

$$\frac{F_{cond}}{F_{rad}} \sim \frac{\mathcal{K}\Delta T}{r\sigma_{SB}T^4} \sim 2 \times 10^{-2}, \quad (7)$$

where at $T = 40\text{--}60\text{ K}$ the thermal conductivity of water ice, the likely dominant component of Arrokoth, $\mathcal{K} \approx 1 \times 10^6 \text{ erg}/(\text{cm}\cdot\text{s}\cdot\text{K})$ (Slack 1980) and we take $T = 60\text{ K}$, $\Delta T = T_{max} - \langle T \rangle = 18\text{ K}$ and $r = 10\text{ km}$. \mathcal{K} of NH_3 ice is about half as large (Krupskii, Manzhely & Koloskova 1968), while \mathcal{K} of methanol glass, the observed surface, but possibly very shallow, constituent, is about $2 \times 10^4 \text{ erg}/(\text{cm}\cdot\text{s}\cdot\text{K})$ (Korolyuk *et al.* 2009). Thermal conduction into and from the deep interior is a minor contributor to the thermal balance of surfaces exposed to sunlight for times $\gg t_{relax}$ while conduction from a layer of thickness $\sim \Delta x$ averages the temperature over a time $\sim t_{relax}$.

In contrast, a surface long exposed to dark space is heated only by conduction through the interior and approaches a steady state temperature T_{dark} given by

$$\sigma_{SB}T_{dark}^4 = \frac{\mathcal{K}(\langle T \rangle - T_{dark})}{r}. \quad (8)$$

The resulting $T_{dark} \approx 23\text{ K}$ is consistent with the measured (Grundy *et al.* 2020; Umurhan *et al.* 2020) dark side temperature of Arrokoth of $29 \pm 5\text{ K}$. However, in superficial layers of thickness $\sim \Delta x$ (Eq. 3) thermal conduction dominates radiative processes on the time scale P_{rot} and is significant on the time scale t_{relax} (Eq. 4).

Because $t_{deep} \gg P_{orb}$, conduction into the deep interior does not significantly affect orbital surface temperature variations; this is implied by Eq. 7. The relevant sublimation rates are very low so the contribution of latent heat to the energy balance is negligible.

The maximum surface temperature is approximately (only approximately, because P_{orb} does not greatly exceed t_{relax}) given by Eq. 1 with $\theta = \pi/2$. This occurs near the pole of the summer hemisphere at solstice (*i.e.*, the sunlit surface as seen in the 2019 New Horizons flyby). At this time the cleft between the lobes, the subject of this paper, is in deep shadow and its temperature approaches $\langle T \rangle$ (Eq. 2) as a result of heat conduction from the interior. The cleft, receiving very little sunlight averaged over an orbit, is a thermal probe of the deep interior.

At equinoxes, the illumination of an ideal wedge-shaped cleft with the Sun aligned with its midplane is shown in Fig. 2. In this geometry the two sides of the cleft come to the same temperature so that radiative exchange between them produces no net heating or cooling; in more complex geometry they come to an average temperature. Averaging over the rotation leads to a mean insolation $I_{\odot} \sin \theta/\pi$. The thermal emission of the cleft and the sunlight it absorbs are both proportional to the area of its mouth so that its *steady state* temperature

$$T_{cleft} = \left(\frac{4}{\pi} \right)^{1/4} \langle T \rangle = 1.062 \langle T \rangle \quad (9)$$

is independent of θ and its width (or depth).

The cleft is illuminated for only a fraction $\sim \theta/\pi$ of the orbit, a time $\sim \theta P_{orb}/\pi \ll t_{relax}$, so this brief period of radiative heating has little effect on its surface temperature. Away from the equinoxes, the cleft is in darkness, without Solar heating, and is a probe into the deep interior, warmed only

Insolation

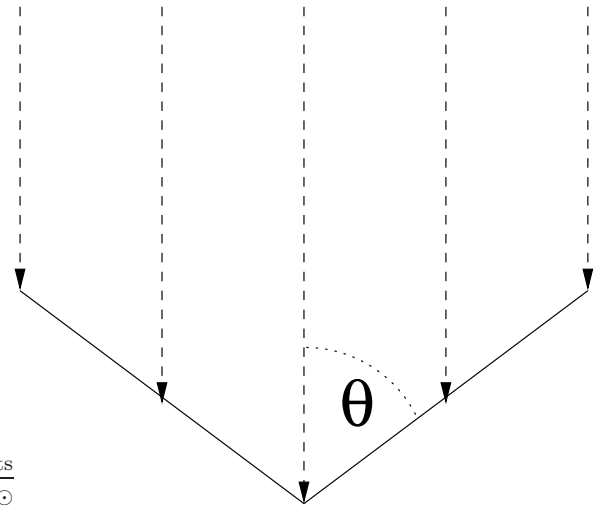


Figure 2. Insolation of a wedge-shaped cleft between the lobes at equinoctial noon. This idealized geometry can only be an approximation to the actual geometry (Grundy *et al.* 2020), but illustrates its essential features.

by heat conduction. Its surface temperature remains closer to $\langle T \rangle$ than does the temperature of any other part of the surface; it has the lowest *maximum* and the highest *minimum* temperature because of its close thermal coupling to the interior. Because of the extreme temperature sensitivity of vapor pressures, accumulation of volatiles is determined by evaporation at the maximum temperature a surface element reaches (evaporation is negligible at any significantly lower temperature, almost regardless of how much lower; Sec. 5.1.3 and Eq. 20), and sublimed volatiles accumulate in the cleft.

At earlier times in the main sequence history of the Sun it was less luminous, so that Arrokoth was colder. Even earlier, the proto-Sun on its Hayashi track (Kippenhahn, Weigert & Weiss 2012) was orders of magnitude more luminous than it is today, so that if Arrokoth had formed then it might have been significantly warmer than it is today. This is complicated by the likelihood that dust in the proto-planetary disc midplane (Kastner *et al.* 1997; Nayakshin *et al.* 2020) made it significantly opaque, reducing the temperature of objects like Arrokoth immersed in it. A further complication is the possibility of heating by short-lived radioactivities (Lisse *et al.* 2021).

3 VAPOR PRESSURES

Even at the low temperatures of Arrokoth, the volatiles He , H_2 , CO , N_2 , O_2 , CH_4 , C_2H_6 and possibly CO_2 are rapidly lost. Arrokoth's escape velocity $v_{esc} \approx 5\text{ m/s}$ if it has the nominal density of 0.5 g/cm^3 (Spencer *et al.* 2020), far below the thermal velocity of any light molecule ($v_{th} \approx 150\text{--}200\text{ m/s}$, depending on molecular weight, at 60 K), so gravity does not much slow their escape (Catling & Zahnle 2009, 2020). The vapor pressures of molecules of possible interest are shown in Fig. 3.

Vapor pressures are calculated from the triple point pressures and the Clausius-Clapeyron equation with one component a perfect gas:

$$\frac{d \ln P_{vap}}{dT} = \frac{L(T)}{k_B T^2}, \quad (10)$$

where $L(T)$ is the latent heat of the phase transition. Not all the required $L(T)$ are available (in particular, for NH_3 hydrate, that we do not consider explicitly). The thermodynamic data have been reviewed and fitted by Fray & Schmitt (2009); for NH_3 from Osborne & Van Dusen (1918); Karwat (1924); Overstreet & Giauque (1937). They have been applied to the long-term stability of Arrokoth's ices by Lisse *et al.* (2021).

The latent heat of sublimation of CO_2 is obtained from Giauque & Egan (1937). The latent heat of sublimation of a solid at its triple point is the sum of the latent heat of melting and that of evaporation of the liquid; hence $L(T)$ is discontinuous at a triple point. This produces small discontinuities in the slopes of the curves in Fig. 3.

When the latent heat is not directly measured (such as at temperatures below the triple point where the vapor pressure is small), it is obtained from the latent heat at a temperature where it is known, typically the triple point, using

$$\frac{dL(T)}{dT} = C_{p,g} - C_{p,s}. \quad (11)$$

The specific heat of NH_3 vapor, $C_{p,g} \approx 4k_B$ per molecule, is that of a classical gas with three rotational but no vibrational degrees of freedom (the rotation constants are, in temperature units, 14.3 K and 8.9 K (Benedict & Plyler 1957), sufficiently below the temperatures of interest). The inversion level spacing of 1.14 K (Popov, Manzhelii & Bagatskii 1971) contributes negligibly to the specific heat. The binding energy of the ammonia dimer (Lee & Park 2000) is about half the latent heat of evaporation of a single molecule; the Saha equation indicates that the fraction of dimers in the saturated vapor at 60 K is about 10^{-7} , so their effect is negligible. At 40 K, the typical temperature of interest, $C_{p,s} \approx 5 \times 10^6$ erg/g-K (Popov, Manzhelii & Bagatskii 1971); for H_2O ice $C_{p,s} \approx 3 \times 10^6$ erg/g-K (Giauque & Stout 1936).

The corrections to $L(T)$ of NH_3 contributed by Eq. 11 amount to only a few percent, and change sign around $T = 129$ K so their effects on the calculated vapor pressure at ~ 60 K approximately cancel. This small correction is not made for other molecules (for most of them correction would not be possible because the specific heats of their solids are not available).

4 SUBLIMATION RATE

A surface (of a pure material) subliming into vacuum loses material at a rate (molecules per unit area per unit time)

$$\dot{N} = \alpha n_{vap} v_{th}, \quad (12)$$

where n_{vap} is the equilibrium vapor number density, v_{th} is its thermal velocity and α is, by detailed balance, the sticking probability of a vapor molecule striking the surface. We adopt $\alpha = 1$, usually a good approximation for surfaces colder than $0.5L/k_B$, in the absence of empirical information. Because of the extreme temperature sensitivity of vapor pressures in the

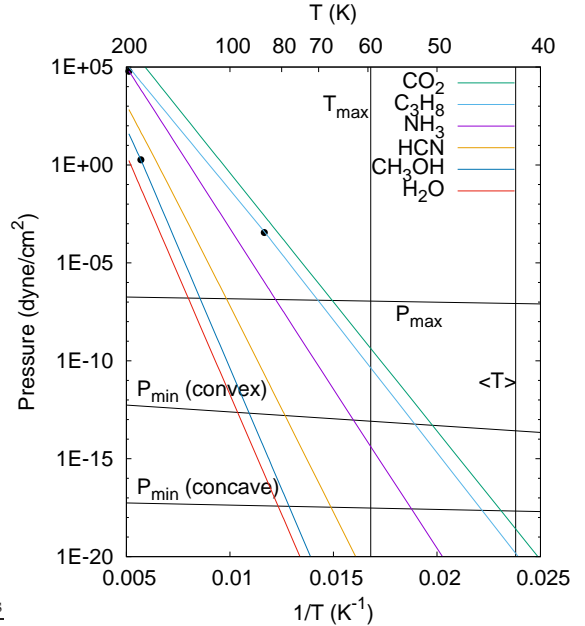


Figure 3. Vapor pressures *vs.* temperature for various possible major component ices of Arrokoth. Curves are in the same order, top to bottom, as the key. The vertical lines indicate $T_{max} = 59.5$ K, the mean (over the orbit) grey-body sub-solar (maximum) steady-state temperature and $\langle T \rangle = 42$ K, the deep interior temperature and temperature of a spherical body of uniform temperature. Vapor pressures above P_{max} would lead to evaporation of an object the size of Arrokoth in the age of the Solar System. Vapor pressures below the geometry-dependent P_{min} could not produce a layer of high albedo pure ices; these vapor pressures are shown for NH_3 but depend slightly on molecular weight through the thermal velocity (Eq. 13). This condition is much less demanding for concave surfaces, such as those showing high albedo in Arrokoth, than for convex surfaces. Consistent with the findings of Lisse *et al.* (2021), the more volatile CO_2 , N_2 and CH_4 are unlikely to be retained to the present day (see discussion in text), while the less volatile CH_3OH , HCN and H_2O are unlikely to provide enough sublimation and redeposition to make the observed regions of high albedo. NH_3 and C_3H_8 could sublime and condense as pure ices on shaded surfaces; NH_3 is likely to be more abundant. Triple points, where the inclusion of the latent heat of melting produces small discontinuities in slope, are indicated by dots; when not shown they are outside the range of the plot. These results are consistent with those of Lisse *et al.* (2021).

relevant temperature ranges, the conclusions are very insensitive to the value of α assumed. The surface recedes at a speed

$$v_{recession} = \frac{\dot{N}}{n_{solid}}, \quad (13)$$

where $n_{solid} \approx 3 \times 10^{22} \text{ cm}^{-3}$ for the simple molecular solids considered here.

The equilibrium vapor number density

$$n_{vap} = \frac{P_{vap}}{k_B T}, \quad (14)$$

where P_{vap} is the equilibrium vapor pressure. Combining these results, the recession rate

$$v_{recession} = \frac{P_{vap} v_{th}}{n_{solid} k_B T} \sim 10^{-4} \frac{P_{vap}}{\text{dyne/cm}^2} \text{ cm/s.} \quad (15)$$

If

$$v_{recession} > v_{max} \sim \frac{r_{Arrokoth}}{t_{\odot}} \sim 10^{-11} \text{ cm/s}, \quad (16)$$

where $t_{\odot} = 1.4 \times 10^{17}$ s is the age of the Solar System as well as that of the Sun, an object the size of Arrokoth is destroyed in less than t_{\odot} . This corresponds to maximum vapor pressure at 60 K of $P_{max} \sim 10^{-7}$ dyne/cm² (scaling $\propto T^{1/2}$).

The vapor pressure of CO₂ is probably too high for it to be retained for the age t_{\odot} of the Solar System because a significant fraction of the surface of Arrokoth may be at temperatures above 50 K (at 55 K a 10 km thickness would evaporate in $0.01t_{\odot}$). It is also evident that the vapor pressures of H₂O and CH₃OH, the latter spectrally identified on Arrokoth (Grundy *et al.* 2020), are too low, as shown by the fact that they are far below either value of P_{min} at any temperature $\leq T_{max}$, to provide sufficient evaporation to deposit a high albedo pure ice.

5 DEPOSITION

Fig. 3 shows the extremely nonlinear sensitivity of vapor pressures to temperature at the temperatures of interest. As a result, evaporation rates are almost entirely determined by the *highest* temperatures a surface encounters. Volatiles condense on the cold-trap surfaces with the lowest maximum temperatures, those in the narrow cleft between the two lobes of Arrokoth, its bright necklace. Any surface exposed to more insolation has a higher peak temperature and sublimation rate. Transfer between these surfaces and the cleft is inefficient in the high vacuum of the present Solar System because most evaporated molecules move faster than escape velocity, but was much more efficient in the proto-Solar System in which the gas density (Desch 2007) was sufficient to make the motion of sublimed molecules diffusive (Sec. 5.2).

A minimum recession rate v_{min} is required for sufficient material to be sublimed to coat the cooler shaded parts of the body, such as the neck between the lobes and the insides of depressions, and to increase their albedo in the age of the Solar System t_{SS} . This layer of deposited pure ice crystals resembling hoarfrost has a high visible albedo if its thickness is $\geq 0.3\lambda$, where λ is the wavelength of Solar radiation (Lock & Laven 2012).

The required minimum recession rate

$$v_{recess} > v_{min} \sim \frac{0.3\lambda}{t_{SS}\eta} \sim 10^{-22} \eta^{-1} \text{ cm/s}, \quad (17)$$

where η is the fraction of evaporated material that is deposited on colder parts of the surface. At low surface temperatures, resublimation may be neglected because of the steepness of the vapor pressure curves. Two cases require consideration:

5.1 Near-Vacuum

We first consider that limit in which the gas density around Arrokoth is so low that evaporated molecules move ballistically, almost never colliding with another molecule.

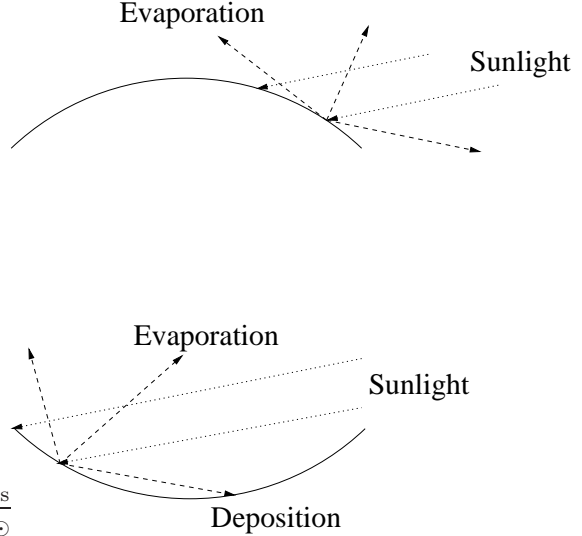


Figure 4. Thermal sublimation from Solar heated convex (above) and concave (below) surfaces in vacuum. Dotted arrows indicate direction of incident sunlight, and dashed arrows the paths of evaporated molecules. Molecules sublimed from concave surfaces, such as the cleft between the lobes of Arrokoth and in depressions or pits may be redeposited, even if the molecules are moving faster than escape speed, as almost all of them do. However, molecules sublimed from convex surfaces faster than escape speed cannot redeposit unless the surrounding gas density is sufficient that their motion is diffusive, as it was in the proto-Solar System. Even in that case, diffusion will produce net transfer from warmer convexities and asperities to cooler concavities, smoothing the surface.

5.1.1 Convex Surfaces

If the surface is convex, only sublimed molecules that have less than escape velocity can return to colder parts of the surface and be deposited, as shown in the upper part of Fig. 4. Because $v_{esc} \ll v_{th}$, Catling & Zahnle (2009, 2020) only a small fraction $\eta \sim (v_{esc}/v_{th})^3 \sim 3 \times 10^{-5}$ (NH₃) or $\sim 1 \times 10^{-4}$ (CO₂) of the sublimed molecules remains gravitationally bound. Only these low velocity molecules, moving ballistically, will strike the surface again. For NH₃

$$P_{vap} > \frac{0.3\lambda n_{solid} k_B T}{t_{SS}\eta v_{th}} \sim 5 \times 10^{-14} \text{ dyne/cm}^2; \quad (18)$$

for CO₂ the required P_{vap} is about 2.5 times less.

5.1.2 Concave Surfaces

The cleft between the two lobes of Arrokoth is concave, as are the insides of depressions. Molecules sublimed from the warmer parts of the surface may strike colder parts, even though their velocities exceed v_{esc} . This is illustrated in the lower part of Fig. 4. Then η may be much higher, perhaps $\mathcal{O}(0.1-1)$, and

$$P_{vap} > 10^{-17} \text{ dyne/cm}^2. \quad (19)$$

5.1.3 Net Deposition

Matter on both the warmer and the cooler parts of the surface will sublime, but the cooler parts will be net gainers of ice if their sublimation rate is $< \eta$ of the evaporation rate of the

warmer parts. This condition will be satisfied if $\Delta T > \Delta T_{min}$, where

$$\Delta T_{min} \approx -\frac{\ln \eta}{d \ln P_{vap}/dT}; \quad (20)$$

for NH_3 at 50 K $d \ln P_{vap}/dT = L/k_B T^2 \approx 1.5/\text{K}$.

For a convex surface in vacuum $\Delta T_{min} \approx 7\text{ K}$. The temperature difference between unshadowed and shadowed parts of the surface likely exceeds this because the mean temperature is 42 K, about 16–19 K below the sub-Solar temperature (Sec. 2.1). For a concave surface in vacuum like the cleft $\Delta T = \mathcal{O}(1\text{ K})$ is sufficient for net deposition on its colder parts.

5.2 Immersed in Gas

As discussed in Sec. 6 and by [Lyra, Youdin & Johansen \(2021\)](#); [McKinnon et al. \(2020\)](#), the rotational state of Arrokoth suggests it was immersed in the gas of the proto-Solar System with a density $\rho_g \sim 4 \times 10^{-11} (2 \times 10^6 \text{ y}/t_{slow})$, where t_{slow} was the time scale on which gas drag slowed its rotation. This process has also been inferred in protoplanetary discs by [Anderl et al. \(2016\)](#); [Öberg et al. \(2017\)](#); [Loomis et al. \(2020\)](#) and in models of the proto-Solar System by [Lesniak & Desch \(2011\)](#); [Krijt et al. \(2018, 2020\)](#); [Mousis et al. \(2019\)](#). The collisional mean free path of a sublimed molecule

$$\ell \sim \frac{m_g}{\rho_g \sigma} \sim 25 \left(\frac{t_{slow}}{2 \times 10^6 \text{ y}} \right) \text{ cm}, \quad (21)$$

where $\sigma \sim 3 \times 10^{-15} \text{ cm}^2$ is a representative molecular collision cross-section and the gas is assumed to have been of Solar composition. This length was orders of magnitude less than the size of Arrokoth if t_{slow} was in the plausible range $10^6\text{--}10^8 \text{ y}$ ([Steckloff et al. 2021](#)). As a result, sublimed molecules did not escape ballistically but rather diffused in the surrounding gas. Colder parts of the surface were effective sinks for diffusing sublimed molecules and the redeposition fraction η may have approached unity. Then (Eq. 20), the temperature difference required for net deposition was small.

This process may also have contributed to the smoothing of the surface of Arrokoth by transporting matter from warmer sunlit convexities to cooler shadowed concavities. Because the maximal possible thermal relaxation time (assuming the highest possible bulk conductivity) t_{relax} (Eq. 4) is a substantial fraction of, but less than, P_{orb} , the highest temperature achieved by a point on the surface (determining the sublimation rate) depends in a continuous manner on the shape, with convex asperities preferentially eroded (in both the ballistic and diffusive regimes). The fact that the cleft between the lobes was not filled indicates that any thermally driven deposition process slowed before the two predecessor bodies came into contact, although the amount of deposition required to make a bright necklace is many orders of magnitude ($\sim 2000 \text{ \AA}/2 \text{ km} \sim 10^{-10}$) less than that required to reshape the body.

A region on which a layer $\gtrsim 0.3\lambda$ thick of ice has been deposited has a much higher visible albedo than a dirty ice surface. The albedo of ice or snow depends on its structure (a continuous solid or many small crystals separated by voids). Analogy with terrestrial water-ice hoarfrost suggests a low density porous structure with an albedo that may approach

unity because of the absence of absorbing mineral matter. Its temperature drops (the magnitude of the decrease depends not only on its albedo but on its proximity to low albedo dirty ice regions, from which heat conducts), accelerating the net deposition of ice.

A surface containing transparent volatiles is subject to an instability in which the volatiles evaporate from warmer, lower albedo, regions and deposit on cooler, higher albedo, regions, further increasing their albedo. Patches of high albedo “hoarfrost” grow at the expense of darker regions. Because of the extreme sensitivity of vapor pressure to temperature, these “hoarfrost” regions will be chemically pure, consisting of only the one chemical species that does not evaporate where it is deposited in the cooler shaded regions while being volatile enough to evaporate from warmer regions.

On a chemically pure surface Solar ultraviolet and cosmic ray irradiation cannot make the darker “tholins” that result from their action on a mixture of carbonaceous and nitrogenous species, forming C–N bonds. The same shadowing mechanism that keeps these regions comparatively cool also reduces the rate at which their material is reprocessed into darker compounds, and may preclude it entirely. Darkening by photochemical reprocessing competes with lightening by vapor deposition of “snows”. Shadowing tilts this competition against darkening, both by reduction of irradiation and by providing a pure, single-species, composition.

6 ROTATION

The rotation period of Arrokoth is 15.92 hours ([Stern et al. 2019](#)). The orbital period of two homogeneous spheres of density ρ in contact, an approximate description of its (imperfectly known) shape, is

$$P_{breakup} = \sqrt{\frac{3\pi}{G\rho} \frac{(1+\zeta)^3}{1+\zeta^3}} \approx 9.2 \text{ h}, \quad (22)$$

where $\zeta = 0.81$ ([Spencer et al. 2020](#)) is the ratio of the spherical equivalent radius of the smaller sphere to that of the larger sphere and a nominal density $\rho = 0.5 \text{ g/cm}^3$, as found for comets and for other small Kuiper Belt Objects ([McKinnon et al. 2020](#); [Spencer et al. 2020](#)), is assumed. If the lobes are not spherical, the mean density of spheres in contact whose centers of masses coincide with those of the lobes should be substituted for ρ (the result would be a good approximation, but not exact). $P_{breakup}$ is the shortest possible rotation period of a strengthless contact binary, and is about 0.6 of the actual rotation period, implying that the contact is in compression. Possible dominant constituents have bulk densities at low temperature ($\text{NH}_3 0.82 \text{ g/cm}^3$ [Blum \(1975\)](#), $\text{H}_2\text{O} 0.92 \text{ g/cm}^3$, $\text{CO}_2 1.6 \text{ g/cm}^3$, $\text{CH}_3\text{OH} 1.02 \text{ g/cm}^3$ ([Davidson 1956](#)), $\text{HCN} 1.04 \text{ g/cm}^3$ ([Rae 1969](#))) higher than the assumed nominal density ρ_{Ar} of Arrokoth; the nominal density, observed for comets, implies a structure with high porosity ([McKinnon et al. 2020](#); [Spencer et al. 2020](#)).

The shape of Arrokoth does not conform to the equipotential (Roche) surfaces of a uniformly rotating fluid with mass concentrated at two orbiting points, in which each lobe is drawn to a singularity at their contact. Nor does it resemble the highly prolate (Jacobi ellipsoid) shape of homogeneous self-gravitating bodies of high angular momentum in equilibrium, such as inferred for ‘Oumuamua ([Meech et al.](#)

2017; Katz 2018) and Haumea (Dunham, Desch & Probst 2019). Nor does it resemble the oblate McLaurin spheroids of lower angular momentum, as suggested for Quaoar (Braga-Ribas *et al.* 2013). This argues against formation models in which a single object was formed by angular momentum-limited accretion (as in an accretion disc like those observed in mass-transfer binary stars) from surrounding gas or particles. The problem of explaining the present state of Arrokoth is the opposite of that of explaining contact and close binary asteroids that are apparently spun up by the YORP effect (that is small in the Kuiper Belt) or by planetary encounters that do not occur for cold classical Kuiper Belt objects in near-circular orbits (Scheeres 2007).

This suggests that the two lobes formed independently as slowly rotating (slower than their breakup rotation rate) objects. Orbiting but separated, their orbit gradually contracted as it lost angular momentum until they came into contact. The long rotation period suggests that some process continued to remove angular momentum after Arrokoth formed, plausibly the same process that also brought its lobes together by removing angular momentum. Even in vacuum, Solar gravity induces Lidov-Kozai oscillations that may bring the lobes into contact (Grishin *et al.* 2020); we only consider processes that are related to the transfer of vapor from one part of the body to another that may explain the bright necklace.

Angular momentum could have been removed by hydrodynamic interaction with surrounding gas in the proto-Solar System (Desch 2007; Lyra, Youdin & Johansen 2021; McKinnon *et al.* 2020). Interaction with gas of density ρ_g produces a torque $\sim \rho_g v^2 r^3 \sim GM_{Ar} \rho_g r^2$, where r is the radius of Arrokoth, its mass is M_{Ar} and the speed of its lobes through the gas $v \sim \sqrt{GM_{Ar}/r}$. Gravitational interaction with the gas produces a comparable characteristic torque $\sim (GM_{Ar}/r^2) M_g r \sim GM_{Ar} \rho_g r^2$. The slowing time

$$t_{slow} \sim \frac{1}{\rho_g} \sqrt{\frac{\rho_{Ar}}{G}} \sim 2 \times 10^6 \left(\frac{\rho_g}{4 \times 10^{-11} \text{ g/cm}^3} \right), \quad (23)$$

where the gas density has been scaled to that of $1 M_{\odot}$ of gas uniformly filling an oblate spheroid of major radii $a = 44$ AU and axial ratio equal to the $2.45^\circ = 0.043$ radian inclination of Arrokoth. The end state of removal of angular momentum by gas drag is consistent with the observed contact binary. This gas is almost entirely hypervolatile hydrogen and helium, and does not condense. Any carbon, nitrogen and oxygen, if not yet reduced to hydrocarbons, ammonia, and water, might condense as CO, N₂ or O₂ but these volatile species would quickly evaporate afterward as the proto-Solar System became transparent to Solar radiation (Glein & Waite 2018; McKinnon *et al.* 2020; Lisse *et al.* 2021; Steckloff *et al.* 2021). In our hypothesis, the bright necklace is produced later.

As the gaseous environment removes angular momentum, bringing the predecessor bodies into contact and then slowing the rotation below the breakup rate (McKinnon *et al.* 2020), so also the proto-Arrokoth exerted a torque on the gas, driving it away, in analogy to the satellite-driven gaps in planetary rings. The end state, a close binary or bilobate single object like Arrokoth, depends on the resupply of gas and therefore on the poorly understood processes of angular momentum transport in the proto-Solar System gas cloud.

7 DISCUSSION

The values of P_{vap} corresponding to recession rates v_{min} and v_{max} are indicated in Fig. 3. NH₃ and C₃H₈ have vapor pressures that would permit deposition of high albedo ice in shaded regions of Arrokoth but low enough that they would not be lost entirely during the age of the Solar System; CO₂ is a marginal member of this class. Of these, NH₃ is expected to be the most abundant and to be a significant constituent of Kuiper Belt objects (Brown 2012). These finely divided ices (snows) have high albedos across the visible spectrum (Pope *et al.* 1992; Hudson *et al.* 2021), consistent with the high albedo of Arrokoth's necklace. The absence of NH₃ in the infrared reflection spectrum of Arrokoth outside the necklace (Grundy *et al.* 2020) may be explained by photochemical processing to “tholins”, also explaining its red color, but the spatial resolution of these spectra was insufficient to constrain the spectrum of any ice in the narrow necklace.

Because of the steep dependence of vapor pressure on temperature at $k_B T \sim L(T)$ (Fig. 3; this is true of any substance when its vapor pressure is small because of the self-similar scaling of the Clausius-Clapeyron equation), sublimation chiefly occurs where the peak insolation is greatest and the maximum temperatures are the highest. Net condensation chiefly occurs where the maximum temperature is the lowest; minimum temperatures make little difference because even at temperatures only slightly less than the highest a subliming region experiences the sublimation rate is negligible. The cleft between the lobes of Arrokoth is sunlit only for brief intervals, of width $\sim P_{orb} \theta / 2\pi$ that may be $\sim 0.03 P_{orb} \sim 10$ y around the equinoxes. Because t_{relax} is comparatively long, the temperature in the cleft remains closer to the deep interior temperature $\langle T \rangle$ than it does anywhere else on the surface. As a result, the cleft traps volatiles sublimed elsewhere as pure ices, giving it a high albedo (and hence yet lower surface temperature), and the bright “necklace” evident in the encounter images (Stern *et al.* 2019).

The fact that Arrokoth consists of two lobes in contact, in contrast to apparently highly prolate 1I/2017 U1 ‘Oumuamua (Meech *et al.* 2017; Bolin *et al.* 2018; ‘Oumuamua ISSI Team 2019), suggests a different origin and history. ‘Oumuamua may have acquired its shape and been expelled from its parent planetary system during a luminous post-main sequence phase of its star (Katz 2018), or it could have been tidally elongated during a close, ejecting passage by a forming exo-Jovian planet (Bolin *et al.* 2018). In analogy to the latter possibility, Arrokoth may have formed and acquired its present configuration within the Kuiper belt when the proto-Solar System was filled with comparatively dense gas within the first $\sim 10^6$ – 10^7 y of the Solar System’s existence (Rieke *et al.* 2005; Mamajek 2009; Richert *et al.* 2018).

The process that smoothed the lobes of Arrokoth must have ceased before they came into contact, because Arrokoth itself retained the deep cleft between its lobes. If $P_{vap} \gg P_{max}$ before the lobes came into contact, then diffusive transport in the comparatively dense proto-Solar System nebula could have effectively smoothed them in much less than the age of the Solar System. The higher temperatures of more insolated convexities and the lower temperatures of more shadowed concavities would round the lobes as matter would preferentially be lost from convexities. This process would have been particularly effective in eroding asperities, that are more open

to insolation and less closely conductively coupled to the interior.

In the comparatively dense gas of the proto-Solar System (Desch 2007) ($n \gtrsim 10^9 \text{ cm}^{-3}$, corresponding to a mass $\sim 10^{30} \text{ g}$, is sufficient to give mean free paths $\lesssim 3 \text{ km}$; Sec. 5.2) so that sublimed molecules do not escape on ballistic trajectories. Instead, they diffuse in the surrounding gas and are readily recondensed on colder surfaces, with η of order unity. The value of η may be comparable to that estimated in Sec. 5.1.2. To produce a high albedo necklace during this phase would require P_{vap} greater than that of Eq. 19 by a factor of 10^3 – 10^4 , the ratio of the age of the Solar System (used in Eq. 19) to the duration of its stage as a dense proto-planetary disc, and numerically similar to the value (Eq. 18) for a convex surface. The dissipation of the proto-Solar System gas cloud meant that sublimed molecules would (except in concavities) almost all escape ballistically rather than redepositing.

These arguments suggest that Arrokoth’s shape, slow spin, and geometry of its necklace formed in the early proto-Solar System. The observed highly reflective and perhaps very thin (sub-micron) hoarfrost necklace may be much younger ($\lesssim 10^8 \text{ y}$). Close passage of luminous stars or nearby supernovae (Stern 2003; Lisse *et al.* 2021) may evaporate an existing thin reflective layer that would be subsequently redeposited. Such shorter ages would imply that the relevant pressures are higher than shown in Fig. 3, but the dependence of vapor pressure on temperature is so steep ($d \ln P_{\text{vap}}/dT \sim 1/\text{K}$) that the changes in the corresponding temperatures would be small. The gradual increase in the Solar luminosity with age produces a similar effect: the vapor pressure of NH_3 at T_{max} has an e -folding time $\sim 3 \times 10^8 \text{ y}$, a time scale that may be more relevant than the age of the Solar System.

APPENDIX

The equilibrium temperature of a Solar System object is determined by the balance between Solar heating and its infrared thermal emission. This depends on its albedo for Solar radiation and its infrared emissivity averaged over a Planck function at its surface temperature. Small bodies in the Kuiper Belt and elsewhere in the outer Solar System, such as Arrokoth (486958; 2014 MU₆₉) and elsewhere in the outer Solar System are made of rock and ices. Vapor pressures are extremely sensitive to temperature at the temperatures $\approx 50 \text{ K}$ found there, so quantitative determination of temperature is necessary to calculate the rate of evaporative loss and vapor transport across their surfaces. This requires quantitative knowledge of the infrared emissivity.

Ammonia ice is of particular interest because in this temperature range its vapor pressure varies from values so low that it is insufficient to deposit sub-micron thick layers on colder parts of a body’s surface in the age of the Solar System to values so large that a 10 km-sized body would not survive that time. In contrast, the vapor pressures of water and methanol ices are so low that evaporation is negligible, while those of methane and even carbon dioxide are so high that they would be lost entirely from a body with negligible gravity.

We use the complex infrared optical constants of ammonia ice (Martonchik, Orton & Appleby 1984) to calculate its reflectivity $R(\nu, \theta, \hat{n})$ as a function of frequency ν , angle of in-

cidence θ and polarization \hat{n} from the Fresnel relations. The emissivity $\epsilon(\nu, \theta, \hat{n}) = 1 - R(\nu, \theta, \hat{n})$.

We assume a homogeneous half-space of solid ammonia; transmitted energy is eventually absorbed, either by the imaginary part of the refractive index (which is very small in most of the spectrum) or by embedded mineral matter (dirt). If this assumption were not made it would be necessary to specify the depth of the ice layer, which is not known, and to match electromagnetic boundary conditions at both interfaces. In fact, the low (≈ 0.1) visible albedo of Arrokoth (Stern *et al.* 2019) implies a deep homogeneous layer of ice in which some mineral matter is embedded; if the ice were finely divided, like snow, the visible albedo would be high because of scattering at interfaces between ice and vacuum (or air, for terrestrial snow).

Once the mean infrared reflectivity $\langle R(T) \rangle$, averaged over a Planck function, is known, the equilibrium temperature may be calculated. There are two simple cases. If sunlight is normally incident with intensity I_{\odot} the steady state temperature is

$$T_{\text{normal}} = \left(\frac{I_{\odot}(1-A)}{\sigma_{SB}(1-\langle R \rangle)} \right)^{1/4}, \quad (24)$$

where A is the Solar albedo, averaged over its spectrum, and σ_{SB} is the Stefan-Boltzmann constant. Averaging over a spherical body yields a mean temperature

$$T_{\text{mean}} = \left(\frac{I_{\odot}(1-A)}{4\sigma_{SB}(1-\langle R \rangle)} \right)^{1/4}, \quad (25)$$

The Fresnel relations for interfaces between dielectric (non-magnetic) materials are

$$R_s = \left| \frac{\sqrt{1-\sin^2 \theta} - \sqrt{n^2 - \sin^2 \theta}}{\sqrt{1-\sin^2 \theta} + \sqrt{n^2 - \sin^2 \theta}} \right|^2 \quad (26)$$

and

$$R_p = \left| \frac{n^2 \sqrt{1-\sin^2 \theta} - \sqrt{n^2 - \sin^2 \theta}}{n^2 \sqrt{1-\sin^2 \theta} + \sqrt{n^2 - \sin^2 \theta}} \right|^2, \quad (27)$$

where s denotes polarization in the plane of incidence, p denotes polarization perpendicular to the plane of incidence and $n(\nu)$ is the complex relative refractive index (the index of the solid when the wave is incident from vacuum).

The mean reflectivity

$$\langle R(T) \rangle = \frac{1}{2} \frac{\int_0^{\infty} d\nu \int_1^0 d\cos \theta [R_s(\nu, \theta) + R_p(\nu, \theta)] F_{\nu}(T)}{\int_0^{\infty} d\nu \int_1^0 d\cos \theta F_{\nu}(T)}, \quad (28)$$

where F_{ν} is the Planck function. While R_s and R_p are properties of the material, $R(T)$ depends on its temperature through $F_{\nu}(T)$. The results are shown in Figures 5–7.

The Planck-averaged emissivity at temperatures of interest for the Kuiper Belt, where solid ammonia is likely to be encountered, is ≈ 0.77 and varies only slightly with temperature. Inclusion of this factor in Eqs. 24 and 25 yields a temperature about 7.5% higher than would be estimated if the body were a black body radiator. The vapor pressure is so sensitive to temperature that this can be significant.

Finely divided ammonia “snow” has higher reflectivity (lower emissivity) because light scatters at every interface between solid and vacuum. This is analogous to the high albedo of terrestrial water-snow. However, it is less extreme, because at wavelengths $\lambda \sim 100\mu$ near the 50 K black body

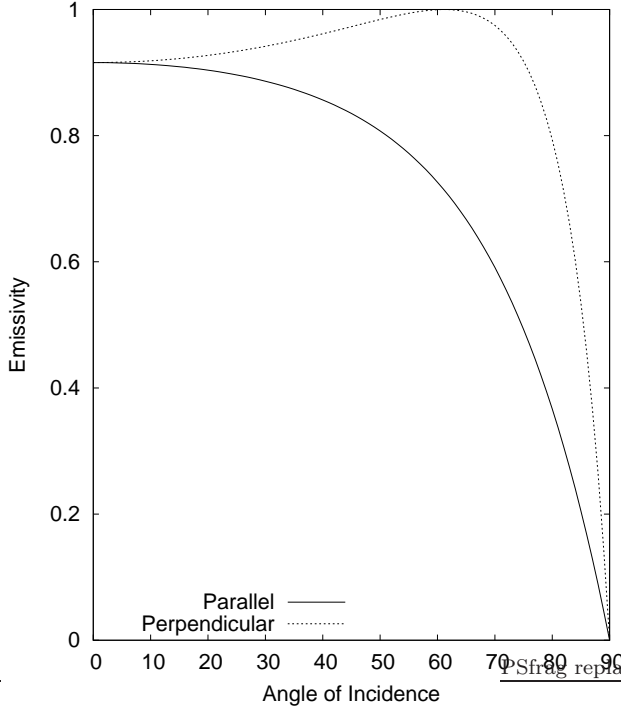


Figure 5. Emissivity ($1 - R$) for infrared radiation with $\lambda = 50\mu$ as a function of angle of incidence.

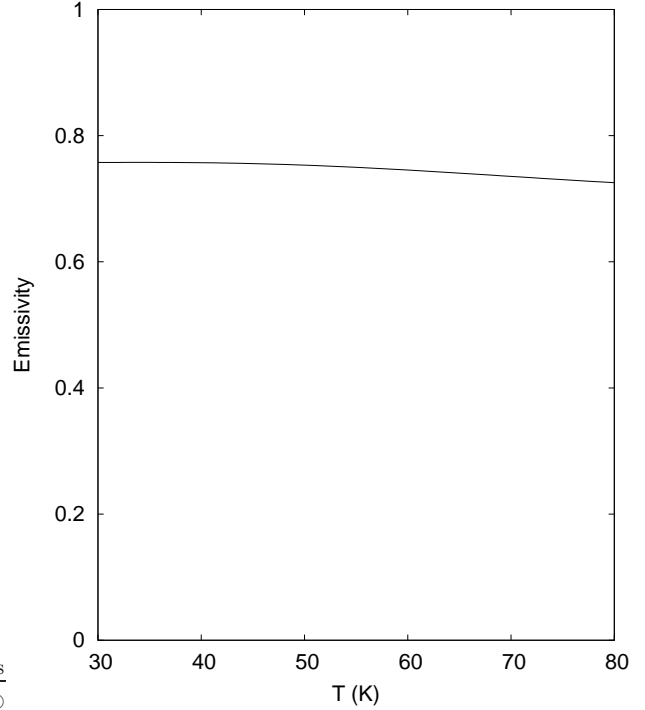


Figure 7. Frequency-integrated emissivity ($1 - \langle R \rangle$) as a function of temperature, averaged over solid angles, polarization and Planck function.

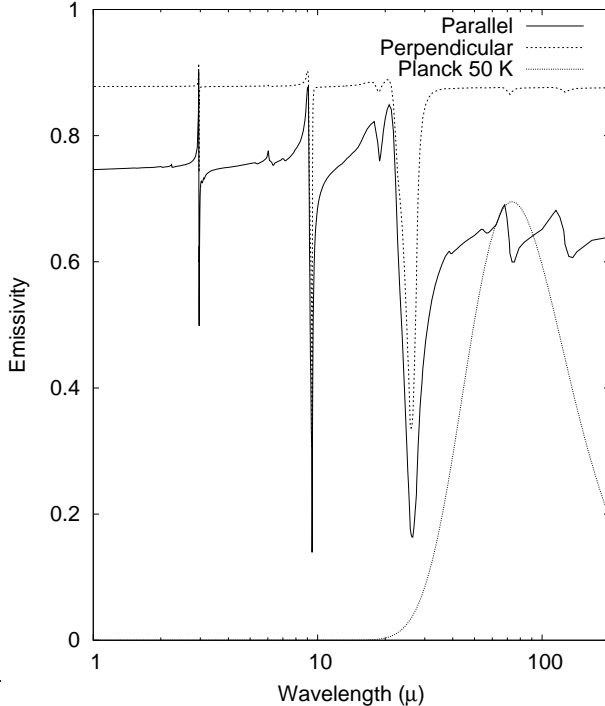


Figure 6. Emissivity ($1 - R$) as a function of wavelength and polarization, averaged over solid angles. The Planck function F_λ at 50 K, with arbitrary normalization, is shown for comparison.

peak the imaginary part of the refractive index $n_i \sim 0.1$ but varies rapidly with λ (Martonchik, Orton & Appleby 1984), suggesting $1 - R \sim 0.1$. Multiple scatterings further reduce R , but a quantitative calculation would require detailed knowledge of the geometry. However, this factor is offset by the fact that the Solar albedo A of pure ammonia snow is likely to be close to unity (Martonchik, Orton & Appleby (1984) give $n_i = 2-4 \times 10^{-5}$ for blue and red light). This is in contrast to the Solar albedo of bulk solid ammonia, which is likely to be small because of mineral or carbonaceous contamination (“dirt”), consistent with the low albedo of Arrokoth. Qualitatively, pure ammonia snow will be significantly cooler than solid ammonia, so that if the the surface is warm enough to evaporate vapor, vapor-deposited ice will accumulate further material at the expense of solid ammonia.

ACKNOWLEDGEMENT

We thank L. M. Canel-Katz, D. Eardley, R. Ogiore, J. R. Spencer and anonymous referees for useful discussions.

DATA AVAILABILITY

This theoretical paper does not contain any new data.

REFERENCES

Anderl, S., Manet, S., Cabrit, S. *et al.* 2016 *A&A* 591A, 3.
Benedict, W. S. & Plyler, E. K. 1957 *Can. J. Phys.* 35, 1235.
Blum, A. 1975 *Radiation Effects and Defects in Solids* 24, 277.

Bolin, B. T., Weaver, H. A., Fernandez, Y. R. *et al.* 2018 *ApJ* 852, L2.

Braga-Ribas, F., Sicardy, B., Ortiz, J. L. *et al.* 2013 *ApJ* 773, 26.

Brown, M. E. 2012 *Ann. Rev. Earth Planet. Sci.* 40, 467.

Catling, D. C. & Zahnle, K. J. 2009 *Scientific American* 300, 36.

Catling, D. C. & Zahnle, K. J. 2020 *Sci. Adv.* 6, eaax1420.

Davidson, D. W. 1956 *Can. J. Chem.* 34, 1243.

Desch, S. J. 2007 *ApJ* 671, 878.

Dunham, E. T., Desch, S. J. & Probst, L. 2019 *ApJ* 877, 41.

Fray, N. & Schmitt, B. 2009 *Plan. Sp. Sci.* 57, 2053.

Giauque, W. F. & Egan, C. J. 1937 *J. Chem. Phys.* 5, 45.

Giauque, W. F. & Stout, J. W. 1936 *J. Am. Chem. Soc.* 58, 1144.

Glein, C. R. & Waite, J. H. 2018 *Icarus* 313, 79.

Grishin, E., Malamud, U., Perets, H. B., Wandel, O. & Schäfer, C. M. 2020 *Nature* 580, 463.

Grundy, W. M., Bird, M. K., Britt, D. T. *et al.* 2020 *Science* 367, eaay3705.

Hofgartner, J. D., Buratti, B. J., Benecchi, S. D. *et al.* 2021 *Icarus* 356, 113723.

Hudson, R. L., Gerakines, P. A., Yarnall, Y. Y. & Coones, R. T. 2021 *Icarus* 354, 114033.

Karwat, E. 1924 *Z. Phys. Chem.* 112, 486.

Kastner, J. H., Zuckerman, B., Weintraub, D. A. & Forveille, T. 1997 *Science* 277, 67.

Katz, J. I. 2018 *MNRAS Lett.* 478, L95.

Kippenhahn, R., Weigert, A. & Weiss, A. 2012 *Stellar Structure and Evolution* 2nd ed. Springer, Berlin.

Korolyuk, O. A., Krivchikov, A. I., Sharapova, I. V. & Romantsova, O. O. 2009 *Fizika Nizkikh Temperatur* 35, 380.

Krijt, S., Schwarz, K. R., Bergin, E. A. *et al.* 2018 *ApJ* 864, 78.

Krijt, S., Bosman, A. D., Zhang, K. *et al.* 2020 *ApJ* 899, 134.

Krupskii, I. N., Manzhely, V. G. & Koloskova, L. A. 1968 *Physica Status Solidi* 27, 263.

Lee, J. S. & Park, S. Y. 2000 *J. Chem. Phys.* 112, 230.

Lesniak, M. V. & Desch, S. J. 2011 *ApJ* 740, 118.

Lisse, C. M., Young, L. A., Cruikshank, D. P. *et al.* 2021 *Icarus* 356, 114072. <https://doi.org/10.1016/j.icarus.2020.114072> arXiv:2009.02277.

Lock, J. A. & Laven, P. 2012 *J. Opt. Soc. Am.* 29, 1489.

Loomis, R. A., Öberg, K. I., Andrews, S. M. *et al.* 2020 *ApJ* 893, 101.

Lyra, W., Youdin, A. N. & Johansen, A. 2021 *Icarus* 356, 113831 arXiv:2003.00670.

Mamajek, E. E. 2009 *AIP Conf. Proc.* 1158, 3.

Martonchik, J. V., Orton, G. S. & Appleby, J. F. 1984 *Appl. Optics* 23, 541.

McKinnon, W. B., Richardson, D. C., Marohnic, J. C. *et al.* 2020 *Science* 367, eaay6620.

Meech, K. J., Weryk, R., Micheli, M. *et al.* 2017 *Nature* 552, 378.

Mousis, O., Ronnet, T. & Lunine, J. I. 2019 *ApJ* 875, 9.

Nayakshin, S., Tsukagoshi, T., Hall, C. *et al.* 2020 *MNRAS* 495, 285.

Öberg, K. I., Guzmán, V. V., Merchantz, C. J. *et al.* *ApJ* 839, 43.

Osborne, N. S. & Van Dusen, M. S. 1918 *Bull. Bur. Stand.* 14, 439.

‘Oumuamua ISSI Team Bannister, M. T., Bhandare, A., Dybczyński, P. T. *et al.* 2019 *Nature Astr.* 3, 594.

Overstreet, R. & Giauque, W. F. 1937 *J. Am. Chem. Soc.* 59, 254.

Pope, S. K., Tomasko, M. G., Williams, M. S., Perry, M. L., Doose, L. R. & Smith, P. H. 1992 *Icarus* 100, 203.

Popov, V. A., Manzelii, V. G. & Bagatskii, M. I. 1971 *J. Low Temp. Phys.* 5, 427.

Porter, S. B., Buie, M. W., Parker, A. H. *et al.* 2018 *Astron. J.* 156, 20.

Rae, A. I. M. 1969 *Mol. Phys.* 16, 257.

Richert, A. J. W., Getman, K. V., Feigelson, E. D. *et al.* 2018 *MNRAS* 477, 5191.

Rieke, G. H., Su, K. Y. L., Stansberry, J. A. *et al.* 2005 *ApJ* 620, 1010.

Scheeres, D. J. 2007 *Icarus* 189, 370.

Slack, G. A. 1980 *Phys. Rev. B* 22, 3065.

Spencer, J. R., Stern, S. A., Moore, J. M. *et al.* 2020 *Science* 367, eaay3999.

Steckloff, J. K., Lisse, C. M., Safrit, T. K., Bosh, A. S., Lyra, W. & Sarid, G. 2021 *Icarus* 356, 113998 arXiv:2007.12657.

Stern, S. A. 2003 *Nature* 424, 639.

Stern, S. A., Weaver, H. A., Spencer, J. R. *et al.* 2019 *Science* 364, 649.

Umurhan, O. M., Keane, J. T., Beyer, R. A. *et al.* 2020 *Bull. AAS* 52 (#235), 419.05

This paper has been typeset from a *T_EX/L_AT_EX* file prepared by the author.